



University
of Glasgow

Chen, G., Tang, L., Yu, Z. and Mace, B. (2021) Mode transition in a standing-wave thermoacoustic engine: a numerical study. *Journal of Sound and Vibration*, 504, 116119. (doi: [10.1016/j.jsv.2021.116119](https://doi.org/10.1016/j.jsv.2021.116119))

This is the author's version of the work. It is posted here for your personal use. You are advised to consult the published version if you wish to cite from it: <https://doi.org/10.1016/j.actaastro.2021.03.010>

<https://creativecommons.org/licenses/by-nc-nd/4.0/>

Copyright © 2021 Elsevier Ltd.

<http://eprints.gla.ac.uk/238287/>

Deposited on: 08 April 2021

Mode transition in a standing-wave thermoacoustic engine: A numerical study

Geng Chen^{1,2,*}, Lihua Tang², Zhibin Yu³, Brian Mace²

1. National Engineering Research Center of Turbo-Generator Vibration, School of Energy and Environment, Southeast University, Nanjing 210096, China
2. Department of Mechanical Engineering, University of Auckland, Auckland 1010, New Zealand
3. James Watt School of Engineering, University of Glasgow, Glasgow G12 8QQ, UK

ABSTRACT

This study investigates the mode transition phenomenon in a standing-wave thermoacoustic engine (TAE) by means of computational fluid dynamics (CFD). Firstly, the steady-state responses of the TAE at selected temperature ratios are examined via continuous wavelet transform. The bifurcation diagram and spectral map indicate that, as the temperature ratio increases, the TAE experiences a series of bifurcations, through which first-mode periodic oscillations, quasiperiodic oscillations and second-mode periodic oscillations occur. Secondly, the TAE performances in the initial decay/build-up, nonlinear saturation and steady states are studied. The onset of the first and/or second acoustic mode is identified via dynamic mode decomposition. The oscillation frequencies and growth/attenuation rates from CFD agree well with those from the reduced-order network model. Nonlinear mode competition takes place during saturation in which the growth of one acoustic mode is affected or even totally inhibited by the growth of the other. At steady state, periodic oscillations exhibit a closed loop in the phase space whilst quasiperiodic oscillations generate a torus. The time-averaged acoustic energy density, acoustic intensity and efficiency increase with increasing temperature ratio. Finally, parametric studies are conducted to investigate the effects of the gap between stack plates and stack position on mode transition. It is found that the TAE will exhibit second-mode oscillations if the stack is near the closed end or the gap is small. Results in this study indicate that mode transition could become a novel approach to match the TAE with external loads for higher electric power outputs.

Keywords: Thermoacoustic engine; Mode transition; Computational fluid dynamics; Continuous wavelet transform; Dynamic mode decomposition;

* Corresponding author: chengeng@seu.edu.cn;

Nomenclature

A	cross-section area (m^2)	<i>Greek symbols</i>	
a	sound speed (m/s)	γ	ratio of isobaric to isochoric specific heats
c	compliance per unit length ($\text{m}^3\text{s}^2/\text{kg}$)	δ	penetration depth (m)
c_p	isobaric specific heat (J/kgK)	ε	dissipation rate
D	diameter of resonator (m)	ζ	time delay (s)
d_s	gaps between stack plates (m)	θ	phase difference
e	specific internal energy (J/kg)	κ	thermal conductivity of fluid (W/mK)
e_{tot}	total energy per unit mass (J/kg)	λ	acoustic wavelength (m)
f	oscillation frequency (Hz)	μ	dynamic viscosity (kg/sm)
$f_{v,k}$	thermo-viscous functions	ρ	density (kg/m^3)
g	thermoacoustic source term	σ	Prandtl number
I	acoustic intensity (kg/s^3)	τ_{ij}	viscous stress tensor
j	$\sqrt{-1}$	ω	angular frequency (rad/s)
k	turbulence kinetic energy	<i>Subscripts</i>	
L	length (m)	0	mean values
l	inertance per unit length (kg/m^5)	1	complex quantity
p	pressure (Pa)	k	thermal effects
Q	heat flow (W)	v	viscous effects
q	heat flux (W/m^2)	<i>Abbreviations</i>	
r_h	hydraulic radius (m)	CFD	computational fluid dynamics
$r_{v,k}$	thermo-viscous resistance ($\text{kg/m}^5\text{s}$)	CWT	continuous wavelet transform
T	temperature (K)	DM	dynamic mode decomposition
t_s	stack plate thickness (m)	D	
u	velocity (m/s)	FFT	Fast Fourier Transform
U	volume velocity (m^3/s)	HPC	high-performance computing
w	acoustic energy density (kg/ms^2)	TAE	thermoacoustic engine
Z	impedance per unit mass ($\text{kg/m}^3\text{s}$)		

1. Introduction

Thermoacoustic engines (TAEs) or prime movers are reciprocating natural heat engines capable of producing substantial acoustic work (up to kW) from low-grade heat sources (as low as 29 °C) such as geothermal energy, industrial waste heat, solar thermal energy and exhaust heat of internal combustion engines [1]. They offer an attractive alternative to exploit low-grade heat by using no or

fewer moving components and environmentally friendly working fluids (e.g., noble and inert gases) [2-4]. The foundation of TAEs is the thermoacoustic effect that arises from the interaction between a compressible fluid and a solid material. Spontaneous oscillations of the compressible fluid (i.e., acoustic waves) will be induced if a threshold temperature gradient is imposed along the solid material [5-7]. Based on the acoustic field, TAEs can be classified into standing-wave and travelling-wave types [8-10]. Standing-wave TAEs rely on imperfect heat conduction to realize Brayton-like thermodynamic cycles within the boundary layers [11-13] whereas travelling-wave TAEs require perfect heat conduction to execute Stirling-like cycles [14-16]. Although standing-wave TAEs are less efficient from a thermodynamic perspective, they are simple in structure, compact in size and, most importantly, cheap to fabricate, therefore remaining competitive with their travelling-wave counterparts regarding cost-effectiveness.

TAEs are essentially acoustic equivalents of traditional gas-cycle heat engines [17]. The working fluid in TAEs undergoes acoustic compression and expansion while simultaneously releasing heat to and absorbing heat from the nearby solid porous material (e.g., stack or regenerator). Unlike traditional heat engines, the period of thermodynamic cycles in TAEs is decided by the natural frequency of the system itself. From an acoustic perspective, TAEs can be viewed as continuous systems that possess multiple acoustic modes. In most cases, the TAE operates at the fundamental mode and that behaviour has been investigated extensively [18-20]. However, under certain circumstances, acoustic oscillations at the fundamental mode may transit to the second or higher modes as the control parameter changes. Such a phenomenon is called *mode transition* in the literature [21]. Mode transition in standing-wave TAEs was first observed in an experimental study by Yazaki et al. [22, 23], where second and higher harmonics were excited together with the fundamental mode in a linear tube with steep temperature gradients, leading to complex quasiperiodic and chaotic oscillations. Similar phenomena were also reported by Atchley [24] and Unni [25], who observed the transition from first-mode oscillations to quasiperiodic and second-harmonic oscillations by controlling the mean pressure and heat input. Mode transition in travelling-wave TAEs was investigated by Biwa [26] and Yu [21]. In their studies, transition between the acoustic mode determined by the looped tube and that decided by the acoustic resonator took place when the heat input or mean pressure was adjusted. Despite being reported in a few studies, mode transition in TAEs has received little attention due to its infrequent appearance in experiments. The underlying mechanism of mode transition and its impact on the performance of the TAE are still not clear at present. Thus, more research on mode transition should be conducted to address the issues stated above.

Previous research on mode transition in TAEs mainly focused on the existence of such phenomena by measuring the steady-state pressure waveforms at different conditions. Although qualitative explanations were made, it is difficult to achieve an in-depth understanding of the mode transition mechanism with limited data obtained from experiments. To address this problem, Chen et al. [27]

performed a system-level theoretical analysis on the stability curves of the acoustic modes inside a standing-wave TAE integrated with an external load. The underlying physics of quasiperiodicity and beating at different external loads was explored from both acoustic and thermodynamic perspectives. Although the stability analysis based on the linear theory enables the prediction of onset temperatures at which the acoustic modes become unstable, it fails to estimate the nonlinear dynamic characteristics of the TAE after onset [28-30]. Computation fluid dynamics (CFD) offers a viable solution to study the nonlinear saturation that occurs before reaching the steady state after onset. The CFD methodology has been successfully implemented to simulate the excitation of the fundamental mode and subsequent evolution to limit-cycle oscillations [31-33]. Nevertheless, there are few reports on the simulation of multiple-mode excitation and competition in TAEs. Therefore, in this study, CFD simulations of unstable thermoacoustic oscillations in the presence of multiple modes are conducted. By means of both frequency- and time-domain analyses, an in-depth understanding of the mode transition process is presented.

This work aims at studying the mode transition phenomenon reported in experiments by performing CFD simulations on a full-scale standing-wave TAE. The simulation results are further interpreted by linear thermoacoustic theory and other signal processing techniques. This rest of paper is organized as follows. Section 2 introduces the computational model and CFD method adopted in this study. Section 3 describes and discusses the mode transition. Section 4 elaborates on the effect of key geometrical parameters on the mode transition. Finally, concluding remarks are made in Section 5.

2. Numerical methods

2.1 Model description

Figure 1(a) illustrates the schematic of the standing-wave thermoacoustic engine (TAE) investigated in the present study. The TAE consists of a hot buffer, a parallel-plate stack that is sandwiched between a pair of hot and ambient heat exchangers (not shown) and an acoustic resonator. Also shown in the figure is the enlarged view of two adjacent solid stack plates. The TAE is closed at the left end ($x = 0$) and open at the right end ($x = L$, $L = L_H + L_S + L_R$), where L_H , L_S and L_R are the lengths of the hot buffer, stack and acoustic resonator, respectively. Geometrical parameters of the baseline TAE model are listed in Table 1.

Figure 1(b) shows the computational domain of the TAE. A full-scale two-dimensional (2-D) model is adopted herein and high-quality structured meshes are generated for the fluid domain. Close-up views of the grid in one stack channel and the near-wall grid in the resonator are presented. Note that exponential bunching laws were employed for mesh generation to ensure that the near-wall grid sizes are smaller than the viscous/thermal boundary layer thicknesses so that the thermoacoustic effect could be captured properly.

Figure 1(c) depicts the mode shapes of acoustic oscillations at the fundamental and second modes. Higher acoustic modes are of no interest in this study and therefore not displayed. Note that, for simplicity, the effects of viscosity and heat conduction on the mode shapes are ignored. For the fundamental mode, the antinodes of acoustic pressure p_{1st} and volume velocity U_{1st} ($U = uA$, where u is the velocity and A is the cross-sectional area) are at $x = 0$ and $x = L$, respectively. In this case, the acoustic wavelength $\lambda = 4L$ approximately. For the second mode, the antinodes of acoustic pressure p_{2nd} and volume velocity U_{2nd} are at $x = 0, 2L/3$ and $x = L/3, L$, respectively. In this case, $\lambda = 4L/3$ approximately.

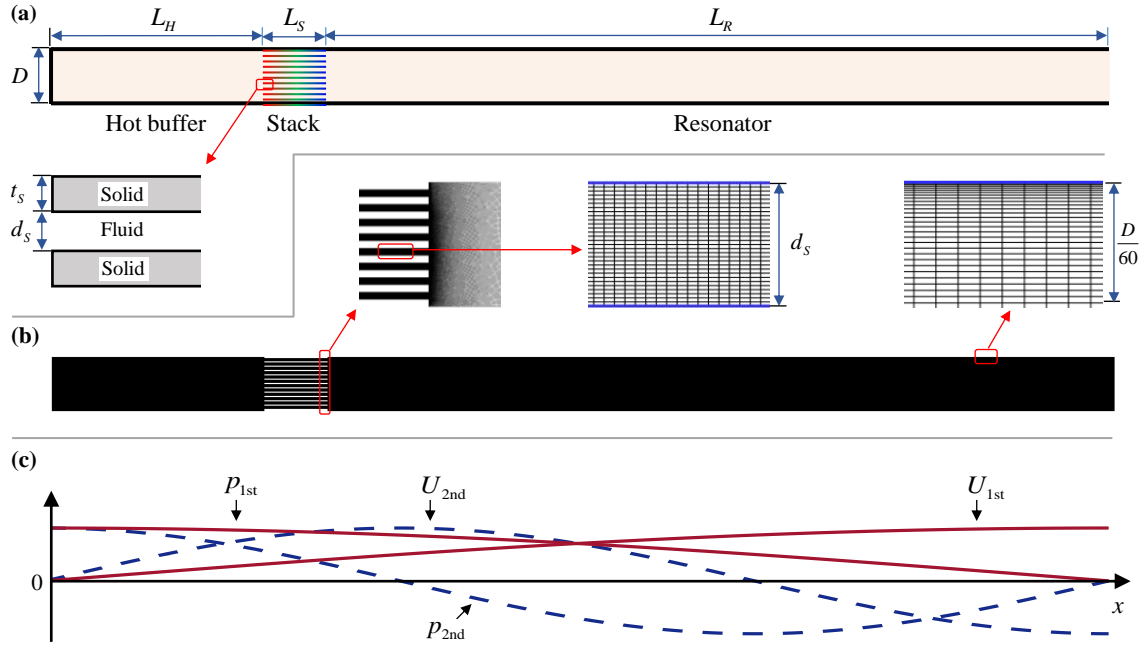


Figure 1. (a) Schematic diagram of the standing-wave TAE. (b) Computational domain (in black) and close-up views of structured grids around the stack end and resonator wall. (c) Mode shapes of acoustic pressure and volume velocity of the fundamental and second modes. The effects of viscosity and heat conduction on the mode shapes are neglected.

Table 1. Geometrical parameters of the baseline TAE model.

Parameters	Values
Diameter D	0.02 m
Hot buffer length L_H	0.1 m
Stack length L_S	0.03 m
Resonator length L_R	0.37 m
Stack plate thickness t_s	1.176×10^{-3} m
Gap between plates d_s	1.176×10^{-3} m

2.2 Governing equations

Computational fluid dynamics (CFD) simulations are performed on the TAE model. Compressible air is chosen as the working fluid and is assumed to be an ideal gas that satisfies the equation of state $p = \rho R_g T$, where p , ρ , T and R_g are pressure, density, temperature and specific gas constant, respectively. In the study of the thermoacoustic oscillations, not only the velocity and pressure fluctuations, but also the density and temperature fluctuations should be taken into account. Therefore, the density weighted time averaging (Favre averaging) approach is employed to deal with the compressible turbulent flows [34]. In Favre decomposition, any dependent fluid variable Φ (e.g., p , ρ , T , etc.) can be expressed as $\Phi = \tilde{\Phi} + \Phi''$ where $\tilde{\Phi} = \overline{\rho\Phi} / \bar{\rho}$ and Φ'' stand for the mean and fluctuating parts, and the overbar “ $\bar{\cdot}$ ” denotes classical time averaging (Reynolds averaging). Substituting these fluid variables into the governing equations of fluid mechanics yields the Favre-averaged Navier-Stokes equations (Einstein summation convention is applied to repeated indices), which are

$$\frac{\partial \bar{\rho}}{\partial t} + \frac{\partial}{\partial x_i} (\bar{\rho} \tilde{u}_i) = 0 \quad (1)$$

$$\frac{\partial}{\partial t} (\bar{\rho} \tilde{u}_i) + \frac{\partial}{\partial x_j} (\bar{\rho} \tilde{u}_i \tilde{u}_j + \bar{p} \delta_{ij} - \tau_{ij}^{tot}) = 0 \quad (2)$$

$$\frac{\partial}{\partial t} (\bar{\rho} \tilde{e}_{tot}) + \frac{\partial}{\partial x_j} (\bar{\rho} \tilde{u}_j \tilde{e}_{tot} + \tilde{u}_j \bar{p} + q_j^{tot} - \tilde{u}_i \tau_{ij}^{tot}) = 0 \quad (3)$$

where u_i or u_j stands for the velocity component in corresponding direction, $e_{tot} = e + u_i u_i / 2$ is the total energy with e being the specific internal energy, and δ_{ij} is the Kronecker delta. The total stress tensor and heat flux are defined as

$$\tau_{ij}^{tot} = \tilde{\tau}_{ij} - \overline{\rho u_i'' u_j''} = (\mu + \mu_t) \left(\frac{\partial \tilde{u}_i}{\partial x_j} + \frac{\partial \tilde{u}_j}{\partial x_i} - \frac{2}{3} \frac{\partial \tilde{u}_k}{\partial x_k} \delta_{ij} \right) - \frac{2}{3} \bar{\rho} k \delta_{ij} \quad (4)$$

$$q_j^{tot} = \tilde{q}_j + c_p \overline{\rho u_j'' T} = -c_p \left(\frac{\mu}{\sigma} + \frac{\mu_t}{\sigma_t} \right) \frac{\partial \tilde{T}}{\partial x_j} \quad (5)$$

where τ_{ij} is the viscous stress tensor and $-\overline{\rho u_i'' u_j''}$ is the Reynolds stress modelled by the Boussinesq hypothesis [35]; μ and μ_t represent the dynamic and turbulent viscosities, and k is the turbulence kinetic energy; q_j is the heat flux given by Fourier's law and $c_p \overline{\rho u_j'' T}$ is the turbulent heat flux modelled by the gradient approximation [35]; σ and σ_t represent the laminar and turbulent Prandtl numbers, and c_p is the isobaric specific heat. Note that $\sigma = \mu c_p / \kappa$, with κ being the heat conductivity. μ , σ and c_p are intrinsic thermophysical properties for a given gas type, while μ_t , σ_t and k have to be calculated using a separate turbulence model. In this study, the standard k - ϵ turbulence model is

adopted to account for turbulence effects. The k - ε model contains two transport equations for the turbulence kinetic energy k and rate of dissipation ε ; $\mu_t = \rho C_\mu k^2 / \varepsilon$ with C_μ being 0.09, while σ_t is set at 0.85 by default [36]. It is worth mentioning that the standard k - ε model has been successfully implemented in previous numerical studies on TAEs and provides reasonable estimates [37-39].

Equations (1) to (3) are resolved numerically using the commercial CFD package FLUENT 18.1 that adopts a pressure-based finite volume method. In the CFD simulations, the PISO (Pressure-Implicit Splitting Operators) scheme is used for pressure-velocity coupling, the second order upwind approach is employed for spatial discretization, and the second-order implicit algorithm is adopted for temporal discretization. The under-relaxation factors for fluid variables are set at default values. In this study, the dynamic viscosity μ is set to obey the Sutherland power law [40] while the thermal conductivity κ is chosen to be 0.242 W/mK in order to obtain sufficient heat exchange from the stack walls [41].

2.3 Initial and boundary conditions

Two steps are implemented consecutively to realize spontaneous thermoacoustic oscillations via CFD [42]. Each step has different initial and/or boundary conditions.

Step 1: steady calculation. In this step, the unsteady terms in Equations (1) to (3) are neglected. Non-slip boundary condition is applied to all wall surfaces. The surface temperatures T_s of the solid hot buffer and resonator are set at T_h and T_c respectively, while T_s of the stack is assumed to decrease linearly from T_h at $x = 0.1$ m to T_c at $x = 0.13$ m. In this paper, T_c is fixed at 300 K but the temperature ratio $\Gamma = T_h / T_c$ varies from 1 to 7. The boundary condition at $x = 0$ is a pressure inlet (gauge pressure 0.1 Pa) while a pressure outlet (gauge pressure 0 Pa) is enabled at $x = L$ (i.e., no acoustic radiation). As a result, non-zero pressure and velocity gradients across the TAE ensue after convergence is obtained in Step 1.

Step 2: transient calculation. In this step, the time dependence of fluid variables is considered and an appropriate time step size is assigned. The resultant flow field (with gradients) from Step 1 serves as the initial condition. As to the boundary conditions, the pressure inlet at $x = 0$ is replaced by a solid wall whereas the others remain the same as Step 1.

2.4 Sensitivity study

The sensitivity of the closed-end ($x = 0$) acoustic pressure to the grid and time step sizes was investigated. In order to find an optimal grid size, the grid size in the stack region was refined, with the number of nodes of the entire mesh being 101,203 (coarse), 173,871 (medium) and 254,832 (fine), respectively. Tests were performed on the baseline model at $\Gamma = 2.2$ and the near-wall grids were refined to ensure $y^+ < 1$. As shown in Figure 2(a), when the number of nodes increases to 173,871, further decreasing the grid size leads to negligible differences in steady-state pressure oscillations. Hence, the optimal node number is chosen as 173,871. Likewise, three time step sizes Δt at 5, 10 and

20 μs were investigated. As shown in Figure 2(b), the pressure oscillations at 20 μs deviate from the other two, whereas the 10 μs shows a good resolution in comparison with the 20 μs . Hence, the optimal time step size is chosen to be 10 μs . To save computational cost, the optimal node number and time step size were adopted for all simulations in Section 3.

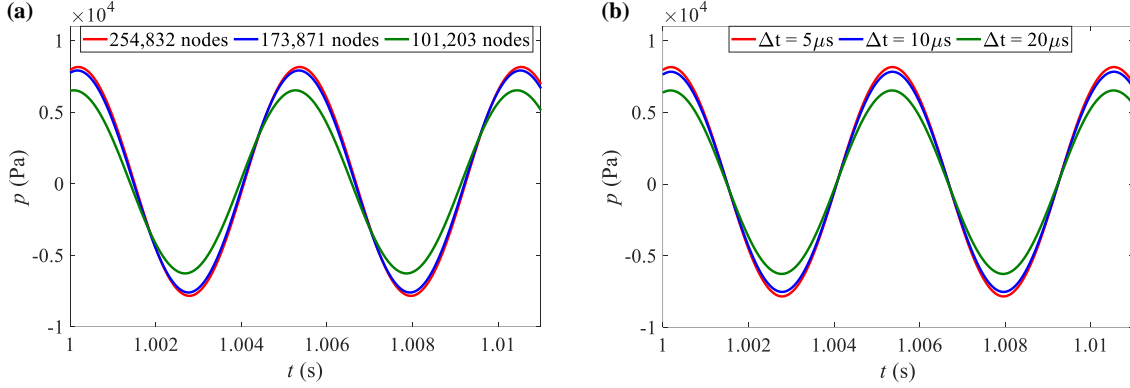


Figure 2. Sensitivity of closed-end acoustic pressure to the (a) number of nodes and (b) time step size Δt . Tests were performed on the baseline model at $\Gamma = 2.2$.

3. Mode transition

3.1 Overview

We first provide an overview of the bifurcation and onset points obtained in this section, as shown in Figure 3. The bifurcation points are identified by the change of the maximum value of pressure oscillations at steady state; the 1st, 2nd and 3rd bifurcations occur at $\Gamma = 1.33$, 3.4 and 6.53, respectively. The onset points are identified by the stability of acoustic modes; the 1st and 2nd onsets occur at $\Gamma = 1.33$ and 2.27. See Sections 3.2 and 3.3 for descriptions of bifurcations and onsets in detail. Also marked on the Γ axis are five temperature ratios Γ_1 to Γ_5 selected as examples for comparison. The values of Γ_1 to Γ_5 are 1.2, 2.2, 2.73, 3.6 and 6.6, respectively.

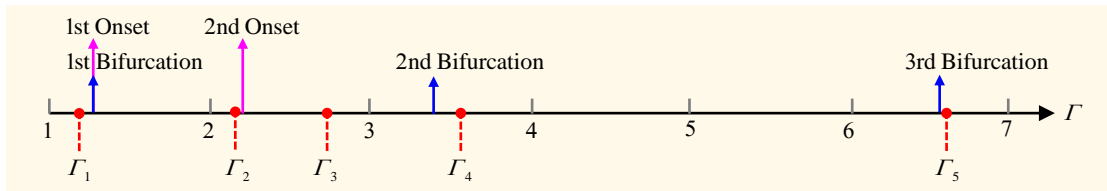


Figure 3. Overview of the bifurcation and onset points along the Γ axis. The 1st, 2nd and 3rd bifurcations occur at $\Gamma = 1.33$, 3.4 and 6.53, respectively; the 1st and 2nd onsets occur at $\Gamma = 1.33$ and 2.27; Γ_1 to Γ_5 are 1.2, 2.2, 2.73, 3.6 and 6.6.

3.2 Description

This section aims to describe the mode transition phenomenon via wavelet transforms, bifurcation diagrams and spectral maps.

3.2.1 Wavelet transforms

Continuous wavelet transform (CWT) [43] is adopted herein to conduct time-frequency analysis of time-varying pressure oscillations. The synchrosqueezing algorithm (using the “wsst” function in Matlab) is selected that reassigns the energy in the frequency direction and preserves the time resolution of acoustic pressure. The wavelet synchrosqueezing contains three steps: (1) obtain the CWT of the input signal; (2) extract the instantaneous frequencies from the CWT output using a phase transform and (3) “squeeze” the CWT over regions where the phase transform is constant.

Figures 4(a) to 4(d) illustrate the time series of the closed-end acoustic pressure and corresponding CWTs at $\Gamma_1, \Gamma_2, \Gamma_4$ and Γ_5 . In Figure 4(a), at $\Gamma_1 = 1.2$, the pressure oscillations decay with time, giving rise to quiescence in the steady state. Most of the acoustic energy is concentrated in the first mode initially and attenuates gradually with time. In Figure 4(b), at $\Gamma_2 = 2.2$, spontaneous pressure oscillations take place, leading to constant-amplitude limit cycles at steady state. The wavelet analysis indicates that the steady-state acoustic pressure is primarily oscillating at the first mode. In Figure 4(c), at $\Gamma_4 = 3.6$, the acoustic field is dominated by the second mode between 0 and 0.2 s. Then, the energy level of the first mode (and second mode) increases (and decreases) from 0.2 s to 0.6 s. Thereafter, the first two acoustic modes co-exist, forming a steady “beating” pattern in the time history. In Figure 4(d), at $\Gamma_5 = 6.6$, the second mode is dominant at all time and the steady-state response returns to limit-cycle oscillations.

3.2.2 Bifurcation diagram

Following the wavelet transforms at the selected values of Γ , we proceed to develop a bifurcation diagram by plotting the maximum value p_{\max} of steady-state closed-end acoustic pressure oscillations versus Γ , as shown in Figure 5. Four regions are identified in line with the four different steady-state responses discussed in Figure 4. In region B-I (quiescence), $\Gamma \in [0, 1.27]$, no acoustic oscillations are initiated (see Figure 4(a)). The first bifurcation occurs at $\Gamma = 1.33$ where the fundamental (or first) mode becomes unstable and produces non-zero p_{\max} . This type of bifurcation is called the Hopf bifurcation in nonlinear dynamics [44]. In region B-II, $\Gamma \in [1.33, 3.33]$, first-mode limit-cycle oscillations dominate at steady state (see Figure 4(b)) and p_{\max} increases with Γ . The second bifurcation occurs at $\Gamma = 3.4$ where the growth of the second mode contributes to a comparable energy level to the fundamental one. This type of bifurcation is also referred to as the Neimer-Saker bifurcation [44]. In region B-III, $\Gamma \in [3.4, 6.47]$, the superposition of the first two acoustic modes leads to an abrupt increase of p_{\max} and exhibits a quasiperiodic (or beat-like) behaviour (see Figure 4(c)). The value of p_{\max} for the quasiperiodic oscillations increases with Γ and levels off after $\Gamma = 5.53$. The third bifurcation occurs at $\Gamma = 6.53$ where the growth of the first mode is totally inhibited, resulting in a sudden drop in p_{\max} . In region B-IV, $\Gamma \in [6.53, 7]$, the second-mode limit-cycle oscillations dominate at steady state (see Figure 4(d)) and p_{\max} increases gradually with Γ .

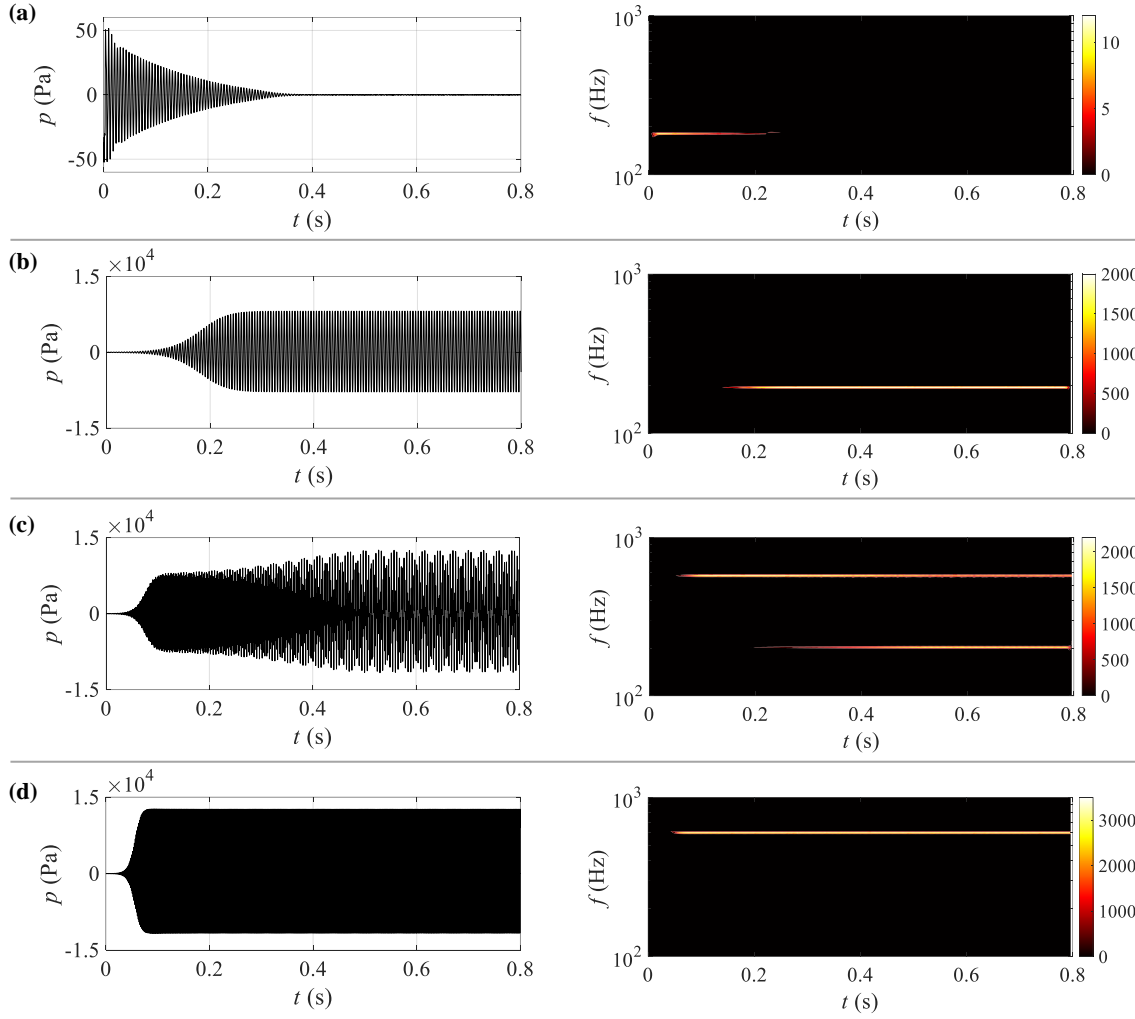


Figure 4. Time history of closed-end acoustic pressure oscillations and corresponding continuous wavelet transform at (a) $\Gamma_1 = 1.2$; (b) $\Gamma_2 = 2.2$; (c) $\Gamma_4 = 3.6$; (d) $\Gamma_5 = 6.6$.

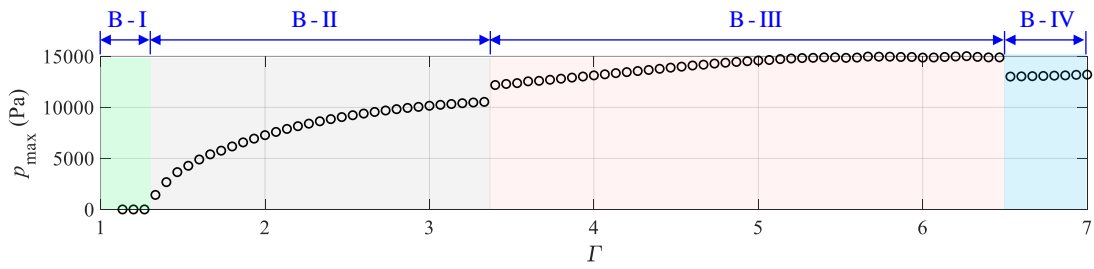


Figure 5. Bifurcation diagram of steady-state responses. Region B-I: Quiescence, $\Gamma \in [0, 1.27]$. Region B-II: Limit cycle (fundamental mode), $\Gamma \in [1.33, 3.33]$. Region B-III: Quasiperiodicity, $\Gamma \in [3.4, 6.47]$. Region B-IV: Limit cycle (second mode), $\Gamma \in [6.53, 7]$.

3.2.3 Spectral map

To facilitate the comprehension of the bifurcation diagram, a 3-D spectral map is constructed. Figure 6(a) plots the spectra of steady-state closed-end acoustic pressure oscillations at different Γ . In region B-I (green lines), no dominant frequencies are observed. In region B-II (black lines), the first-mode

frequency f_1 dominates. In region B-III (red lines), there are significant spectral components at both f_1 and the second-mode frequency f_2 . In region B-IV (blue lines), the dominant frequency becomes f_2 .

Figure 6(b) displays the amplitudes $p_{A,1}$ and $p_{A,2}$ of the first two modes extracted from the spectral map. For any value of Γ , $p \approx p_{A,1}\cos(2\pi f_1 t + \theta_1) + p_{A,2}\cos(2\pi f_2 t + \theta_2)$. Since $f_1 \neq f_2$, $p_{\max} \approx p_{A,1} + p_{A,2}$. Taking $\Gamma_4 = 3.6$ as an example, $p_{A,1}$ and $p_{A,2}$ are 6788 and 5770, and their sum, i.e., 12558, approximates $p_{\max} = 12550$. It is interesting to observe that, $p_{A,1}$ and $p_{A,2}$ experience sudden changes at three bifurcation points. In region B-III, when Γ increases, $p_{A,1}$ decreases and $p_{A,2}$ increases, reflecting the energy transition from the first mode to the second mode.

Figure 6(c) illustrates the variation of f_1 and f_2 extracted from the spectral map. Since f_1 after the third bifurcation and f_2 before the second bifurcation are not initiated, their values are not displayed. In all regions, f_1 and f_2 increase with Γ due to the increase of sound speed. In region B-III, f_1 and f_2 are incommensurate. The ratio f_2 / f_1 varies with Γ and is less than 3, being typically 2.85. Hence, the second mode in this study is different from the second harmonic which would occur at $3f_1$ at large amplitudes.

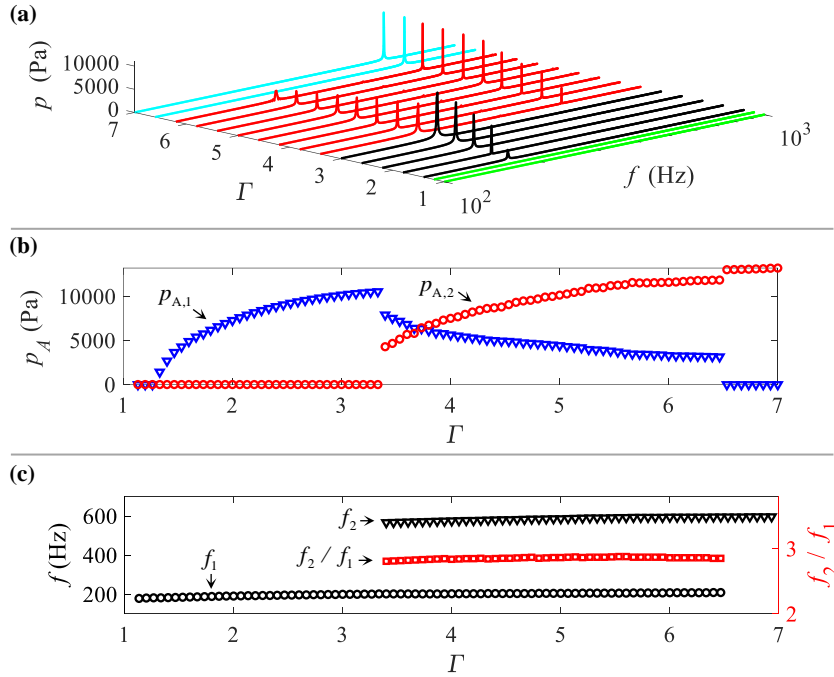


Figure 6. (a) Spectral map. (b) Dependence of $p_{A,1}$ and $p_{A,2}$ on Γ . (c) Dependence of f_2 and f_1 as well as their ratio f_2/f_1 on Γ .

3.3 Discussion

The acoustic pressure undergoes initial decay/build-up and/or nonlinear saturation before reaching steady state. These processes are discussed separately in this section to deepen the understanding of the mode transition phenomenon.

3.3.1 Initial decay or build-up

The initial decay/build-up refers to the very short period after the transient simulation starts. In this process, the pressure amplitude is relatively small so that its dynamic behaviour can be modelled by the linear thermoacoustic theory.

Consider CFD simulations on the baseline model at Γ_1 and Γ_3 shown in Figure 7. In Figure 7(a), when $\Gamma_1 = 1.2$, the decaying acoustic pressure contains multiple acoustic modes. Since the energy level decreases dramatically for higher modes, we focus our attention on the first two modes, the responses of which are obtained through dynamic mode decomposition (DMD). The “highpass filter” in Matlab is used to realize DMD. In the filter design, the filter order is 20, the sampling frequency is 10^5 Hz, and the passband frequency is set as 400 Hz. Applying curving fitting (using exponential equations and the nonlinear least squares method) to the local pressure maxima and Fast Fourier Transform (FFT) to the decomposed signals yields the $\omega_{I,1}$ and $\omega_{R,1} / 2\pi (= f_1)$ for the first mode, and $\omega_{I,2}$ and $\omega_{R,2} / 2\pi (= f_2)$ for the second mode. $\omega_{I,1}$ and $\omega_{I,2}$ are growth/attenuation rates, while $\omega_{R,1}$ and $\omega_{R,2}$ are oscillation frequencies. In Figure 7(b), when $\Gamma_3 = 2.73$, the first two acoustic modes are both initiated. Likewise, implementation of curve fitting and FFT to the pressure signals after DMD gives the $\omega_{I,1}$, $\omega_{I,2}$, $\omega_{R,1} / 2\pi$ and $\omega_{R,2} / 2\pi$ for both cases. From Figures 7(a) and 7(b), one can also imagine the decomposition of acoustic pressure oscillations at $\Gamma_2 = 2.2$ where the first acoustic mode is initiated but the second mode is not. For brevity, those results are not displayed.

The attenuation/growth rates and oscillation frequencies can also be predicted by the reduced-order network model based on linear thermoacoustic theory [45-47]. The network model (see Appendix A for a detailed description) has been experimentally validated in our previous study [46]. Comparison is made between the CFD simulations (discrete dots) and theoretical estimates (solid lines) as shown in Figure 8. It is found that the linear theory predicts slightly higher values of ω_R . Good agreement is achieved for $\omega_{I,1}$ while small deviations are observed for $\omega_{I,2}$ at some Γ . Overall, the linear theory matches well with the CFD simulations. Also highlighted in Figure 8 are three regions classified by the sign (positive or negative) of $\omega_{I,1}$ and $\omega_{I,2}$. In region O-I, $\Gamma \in [0, 1.27]$, $\omega_{I,1} > 0$, $\omega_{I,2} > 0$, which means that pressure oscillations at the first two modes decay exponentially with time. The onset of the first mode occurs at $\Gamma = 1.33$. Hence, in region O-II, $\Gamma \in [1.33, 2.2]$, $\omega_{I,1} < 0$, $\omega_{I,2} > 0$, indicating the growth of the first mode and attenuation of the second mode. The onset of the second mode occurs at $\Gamma = 2.27$. Hence, in region O-III, $\Gamma \in [2.27, 7]$, $\omega_{I,1} < 0$, $\omega_{I,2} < 0$, leading to exponential growth of first two modes. It is worth noting that region O-II in Figure 8 is narrower than region B-II in Figure 5. The difference is attributed to the mode competition in the nonlinear saturation process as will be discussed in the next section.

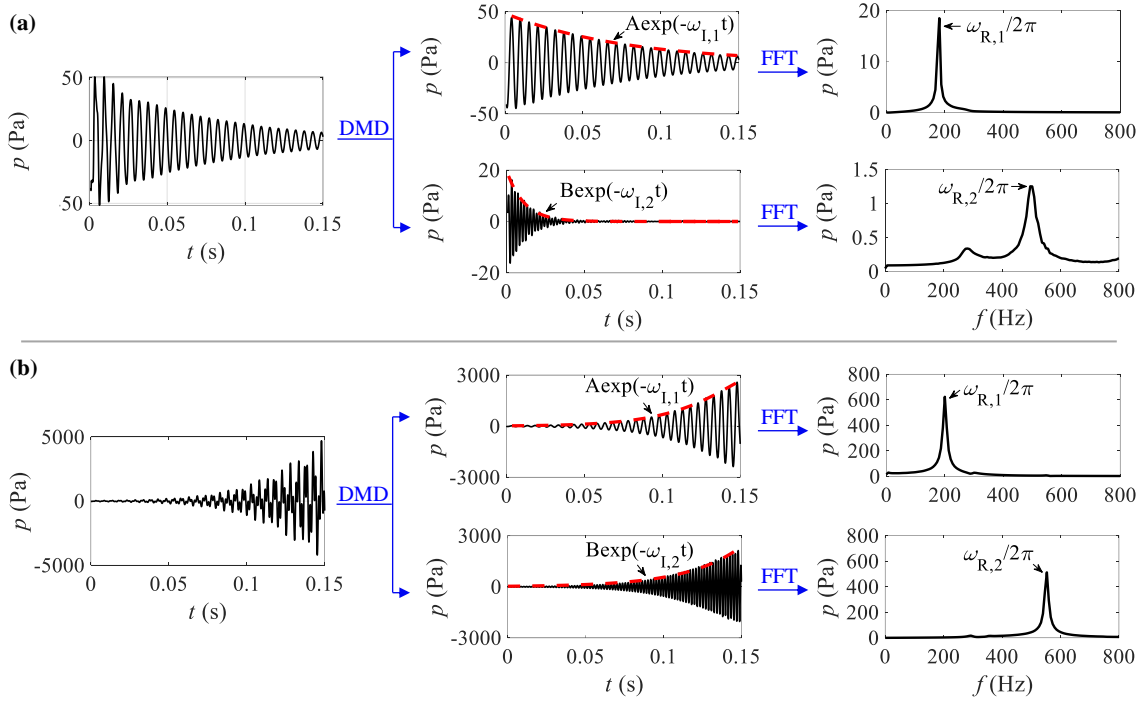


Figure 7. Decomposition of closed-end acoustic pressure oscillations in the initial decay/build-up at (a) $\Gamma_1 = 1.2$ and (b) $\Gamma_3 = 2.73$.

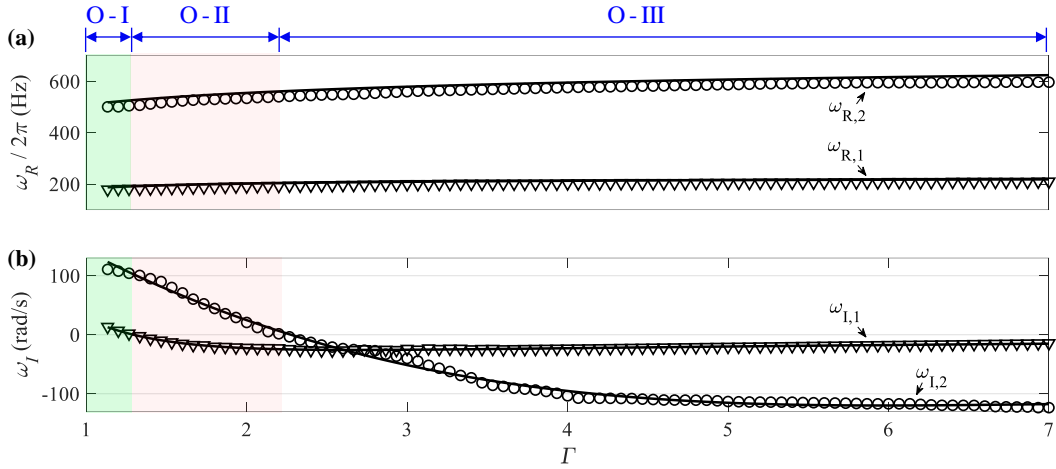


Figure 8. Dependence of ω_1 and ω_R on Γ in the initial decay/build-up. Solid lines are from the linear theory. Discrete dots are from CFD simulations. Region O-I: $\Gamma \in [0, 1.27]$, $\omega_{1,1} > 0$, $\omega_{1,2} > 0$. Region O-II, $\Gamma \in [1.33, 2.2]$, $\omega_{1,1} < 0$, $\omega_{1,2} > 0$. Region O-III, $\Gamma \in [2.27, 7]$, $\omega_{1,1} < 0$, $\omega_{1,2} < 0$.

3.3.2 Nonlinear saturation

Nonlinear saturation refers to the period in which the amplitude of acoustic pressure deviates from exponential growth and asymptotes towards a constant value. From an energy point of view, the increase of pressure amplitude induces nonlinear viscous and thermal-relaxation losses that balance the acoustic power generation in the stack region. The sources of nonlinearity in TAEs include minor losses at the stack ends, mass streaming, onset of turbulence within the boundary layers, and so on [1].

Since theoretical modelling of those nonlinearities is difficult and challenging, we resort to the CFD methodology to investigate the complicated mode competition in the saturation process.

Figures 9(a), 9(d), 9(g) and 9(j) plot the time histories of closed-end acoustic pressure at Γ_2 , Γ_3 , Γ_4 and Γ_5 , respectively. The nonlinear saturation falls into the (green) shaded area. Figures 9(b), 9(e), 9(h) and 9(k) are the corresponding first-mode components whilst Figures 9(c), 9(f), 9(i) and 9(l) are the corresponding second-mode components. In Figure 9(a), when $\Gamma_2 = 2.2$, only the first mode is initiated. In Figure 9(d), when $\Gamma_3 = 2.73$, the first two modes are both initiated at the beginning. However, the first-mode acoustic pressure inhibits the second mode to death as it saturates. As a result, only first-mode pressure oscillations are retained after saturation. In Figure 9(g), when $\Gamma_4 = 3.6$, the energy levels of the first two modes are comparable. The growth of first-mode pressure oscillations relates to the decay of the second mode during the saturation process. In Figure 9(j), when $\Gamma_5 = 6.6$, although the first two modes are both initiated initially, only the second mode is retained after saturation due to the inhibition of first-mode pressure oscillations to death as shown in the enlarged view in Figure 9(k).

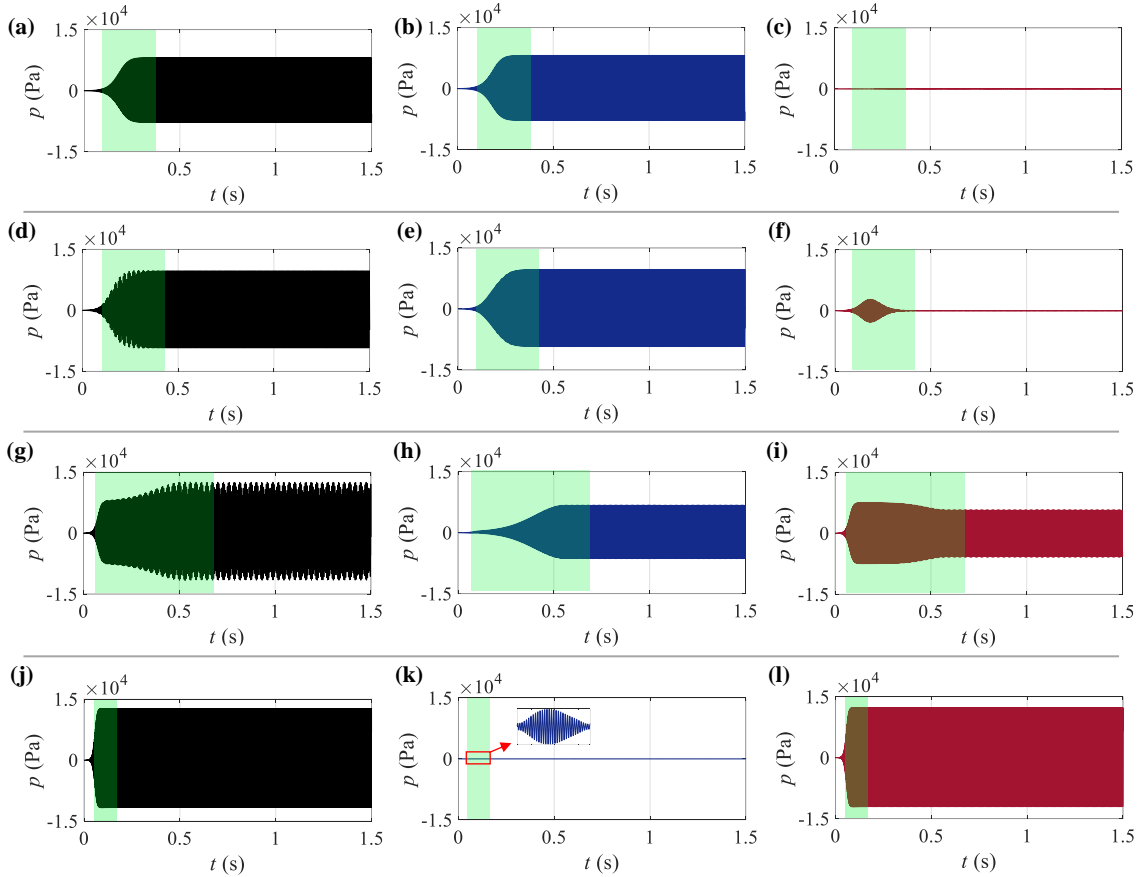


Figure 9. Decomposition of closed-end acoustic pressure oscillations at (a) $\Gamma_2 = 2.2$; (d) $\Gamma_3 = 2.73$; (g) $\Gamma_4 = 3.6$; (j) $\Gamma_5 = 6.6$; (b), (e), (h) and (k) are the corresponding first-mode components whilst (c), (f), (i) and (l) are the corresponding second-mode components.

3.3.3 Steady state

The steady state refers to the period where the acoustic power generation in the stack is balanced by the losses in the remainder of the system. Phase space trajectories, acoustic energy density, acoustic intensity, heat fluxes and efficiency are discussed in this section to explore the TAE performance at steady state.

3.3.3.1 Phase space trajectories

The phase space is often used to analyse the dynamic behaviour of a mechanical system [48]. For the TAE in this study, the steady-state closed-end acoustic pressure waveforms at Γ_2 , Γ_4 and Γ_5 are shown in Figures 10(a), 10(c) and 10(e), respectively. Figures 10(b), 10(d) and 10(f) plot corresponding 3-D phase space trajectories, in which the time delay ζ is chosen as 10^{-3} s [49]. At $\Gamma_2 = 2.2$, periodic pressure oscillations in the first mode form a single loop in the phase space. So does the acoustic pressure at $\Gamma_5 = 6.6$ but here the period is that of the second mode. At $\Gamma_4 = 3.6$, however, the pressure oscillations are aperiodic since there are two incommensurate frequencies present in the system. In such case, the attractor is a torus described by two circles, and the trajectories of the state point in the phase space will evolve on the surface of the torus [50].

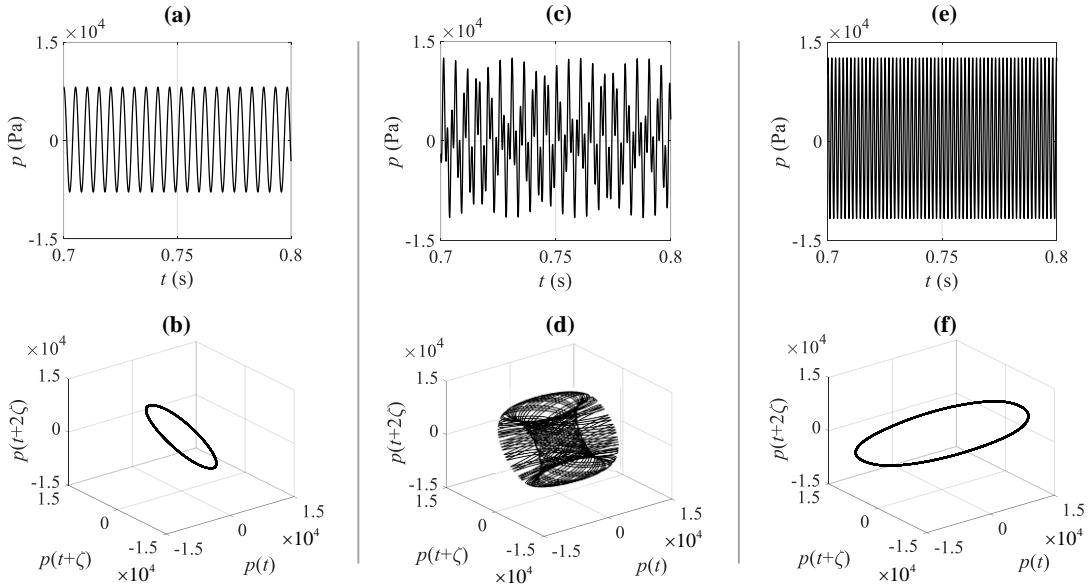


Figure 10. Steady-state closed-end acoustic pressure waveforms at (a) $\Gamma_2 = 2.2$, (c) $\Gamma_4 = 3.6$ and (e) $\Gamma_5 = 6.6$. (b), (d) and (f) are corresponding phase space trajectories.

3.3.3.2 Acoustic energy density

The instantaneous acoustic energy density often used to represent the mechanical energy of a sound wave is expressed by

$$w = \frac{1}{2} \rho_0 \left(u^2 + \frac{1}{\rho_0^2 a^2} p^2 \right) \quad (6)$$

where ρ_0 is the density of the static medium, u is the velocity in x direction and a is the local sound speed. For the standing-wave TAE in this study, the acoustic field is dominated by standing waves. Then, the acoustic pressure and velocity can be approximated by

$$p = \sum_{i=1}^n p_{A,i} \cos\left(\frac{\omega_i}{a} x\right) \cos(\omega_i t); \quad u = \sum_{i=1}^n \frac{p_{A,i}}{\rho_0 a} \sin\left(\frac{\omega_i}{a} x\right) \sin(\omega_i t) \quad (7)$$

For a single acoustic mode, the time-averaged acoustic energy density \bar{w} is

$$\bar{w} = \frac{1}{4} \frac{p_A^2}{\rho_0 a^2} \left(\sin^2\left(\frac{\omega}{a} x\right) + \cos^2\left(\frac{\omega}{a} x\right) \right) = \frac{1}{4} \frac{p_A^2}{\rho_0 a^2} \quad (8)$$

When two acoustic modes co-exist, \bar{w} becomes

$$\begin{aligned} \bar{w} &= \frac{1}{4} \frac{p_{A,1}^2}{\rho_0 a^2} + \frac{1}{4} \frac{p_{A,2}^2}{\rho_0 a^2} + \frac{1}{2} \frac{p_{A,1} p_{A,2}}{\rho_0 a^2} \sin\left(\frac{\omega_1}{a} x\right) \sin\left(\frac{\omega_2}{a} x\right) \overline{\sin(\omega_1 t) \sin(\omega_2 t)} + \\ &\quad \frac{1}{2} \frac{p_{A,1} p_{A,2}}{\rho_0 a^2} \cos\left(\frac{\omega_1}{a} x\right) \cos\left(\frac{\omega_2}{a} x\right) \overline{\cos(\omega_1 t) \cos(\omega_2 t)} \\ &= \frac{1}{4} \frac{p_{A,1}^2}{\rho_0 a^2} + \frac{1}{4} \frac{p_{A,2}^2}{\rho_0 a^2} = \bar{w}_1 + \bar{w}_2 \end{aligned} \quad (9)$$

Figure 11 illustrates w at $x = 0$ from the simulations. Since $u = 0$ at $x = 0$, only the p^2 term in Equation (6) is non-zero, and w is always positive. In Figure 11(a), at $\Gamma_2 = 2.2$, w is primarily oscillating at $2f_1$, however, the amplitude is not constant. FFT and DMD analyses (not displayed) reveal that a small component at f_1 exists due to non-zero mean pressure p_0 induced during nonlinear saturation. In Figure 11(b), at $\Gamma_4 = 3.6$, w exhibits a beat-like pattern. FFT analysis indicates that w is dominated by $2f_1$ and $2f_2$, however, there also exist small components at f_1 and f_2 because p_0 is non-zero.

Figure 12 shows the dependence of \bar{w} on Γ . Figure 12 is similar to Figure 5 except at $\Gamma = 3.4$ and 6.53 where \bar{w} undergoes a sudden drop and a sudden increase, respectively. The difference is caused by the incoherence of the standing waves at the first two modes. More specifically, it is because the $\overline{\sin(\omega_1 t) \sin(\omega_2 t)}$ and $\overline{\cos(\omega_1 t) \cos(\omega_2 t)}$ terms in Equation (9) are zero. Take $\Gamma = 3.33$ in region B-II and $\Gamma = 3.6$ in region B-III as examples. Although $p_{A,1} + p_{A,2} = 12519$ at $\Gamma = 3.6$ is larger than $p_{A,1} = 10540$ at $\Gamma = 3.33$, $p_{A,1}^2 + p_{A,2}^2 = 7.9 \times 10^7$ at $\Gamma = 3.6$ is smaller than $p_{A,1}^2 = 1.11 \times 10^8$ at $\Gamma = 3.33$. This explains why \bar{w} at $\Gamma = 3.6$ is smaller than that at $\Gamma = 3.33$.

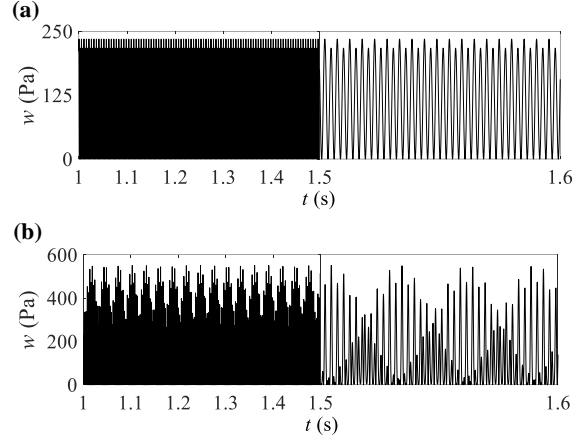


Figure 11. Instantaneous acoustic energy density w at $x = 0$ at (a) $\Gamma_2 = 2.2$ and (b) $\Gamma_4 = 3.6$. Note the split time scales.

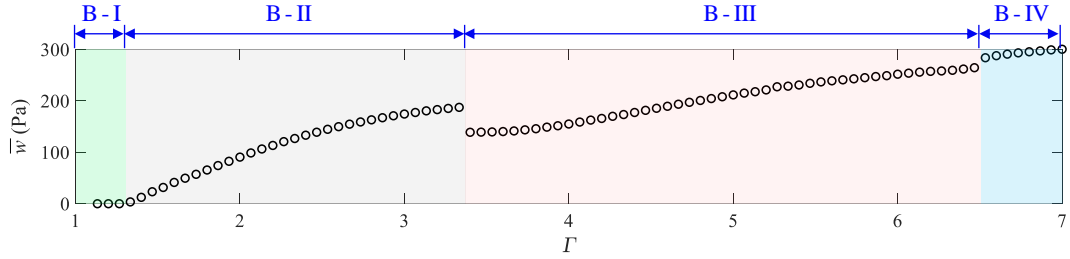


Figure 12. Dependence of time-averaged acoustic energy density \bar{w} at $x = 0$ on Γ .

3.3.3.3 Acoustic intensity

The instantaneous acoustic intensity

$$I = pu \quad (10)$$

can be interpreted as the ability of a slab of gas to do work on the gas adjacent to it. The time-averaged acoustic intensity \bar{I} represents the net work done by the gas in a period. $\bar{I} = 0$ in a standing wave. Thus, it is the travelling-wave component within the viscous and thermal boundary layers that contributes to a non-zero \bar{I} . TAEs rely on $\Delta\bar{I}$ generated in the stack to overcome the thermal and viscous losses and to drive the external loads.

Figure 13 shows the instantaneous ΔI across the stack at steady state at Γ_2 and Γ_4 , respectively. In contrast to w , ΔI can be negative. However, the magnitude of ΔI_{\max} is larger than that of ΔI_{\min} , indicating a positive $\Delta\bar{I}$. In Figure 13(a), ΔI is primarily oscillating at $2f_1$, accompanied by a small component at f_1 due to non-zero p_0 . In Figure 13(b), ΔI is primarily oscillating at $2f_1$ and $2f_2$, accompanied by small components at f_1 and f_2 . Figure 14 plots the dependence of $\Delta\bar{I}$ across the stack on Γ . Generally, $\Delta\bar{I}$ increases with increasing Γ . $\Delta\bar{I}$ also decreases and increases suddenly at $\Gamma = 3.4$ and 6.53 due to incoherent travelling waves at incommensurate frequencies.

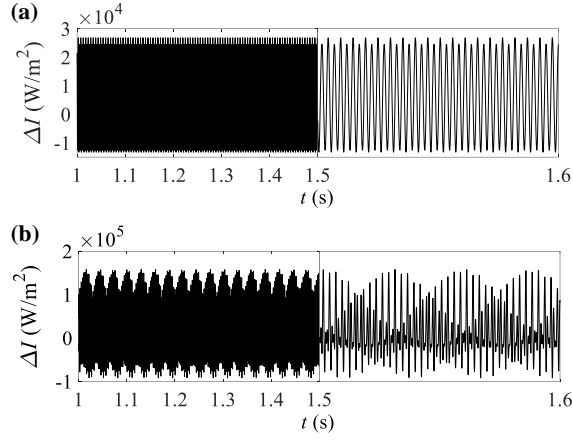


Figure 13. Instantaneous acoustic intensity generation ΔI in the stack at (a) $\Gamma_2 = 2.2$ and (b) $\Gamma_4 = 3.6$.

Note the split time scales.

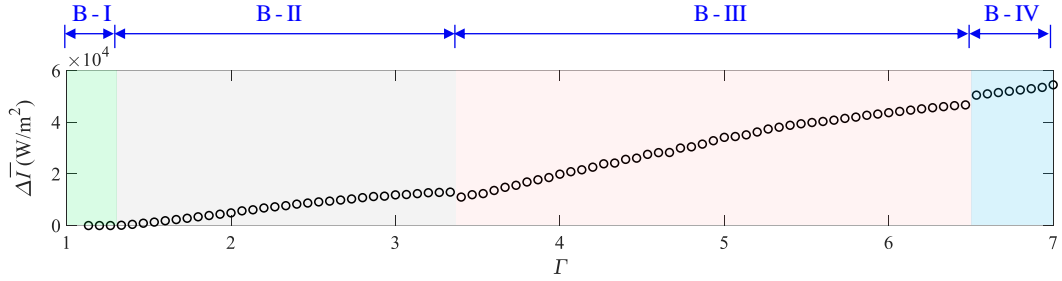


Figure 14. Dependence of time-averaged acoustic intensity generation $\Delta \bar{I}$ across the stack on Γ .

3.3.3.4 Heat fluxes and efficiency

The heat fluxes at the wall surfaces underlies the generation of acoustic intensity. To investigate the heat fluxes, the time-averaged mean temperature T_0 of the oscillatory fluid at $\Gamma_2 = 2.2$ is first examined, as shown in Figure 15(a). In the simulation, the surface temperature of the stack T_s is set to decrease from 660 K at $x = 0.1$ m to 300 K at $x = 0.13$ m. However, T_0 is smaller than T_s in the left half of the stack, but becomes larger in the right half. In addition, due to the vortex shedding at the stack ends, the T_0 around the stack left (or right) end is also smaller (or larger) than T_s .

The deviation of T_0 from T_s leads to non-zero heat fluxes at the wall surfaces, as shown in Figure 15(b). In the figure, the time-averaged transversal heat flux \bar{q}_t is calculated by

$$\bar{q}_t = -\kappa \left. \frac{\partial T_0}{\partial n} \right|_{\text{surface}} \quad (11)$$

where n represents the direction normal to the wall surfaces. A positive \bar{q}_t indicates heat absorption by the fluid while a negative \bar{q}_t denotes heat release to the walls. We can see from the figure that, in the stack region, most of the heat supplied by the left-half stack walls is extracted by the right-half

stack walls. Then, the thermal-to-acoustic efficiency η of the stack (not the TAE) can be coarsely estimated by

$$\eta = \frac{\sum \int_{0.1}^{0.115} \bar{q}_{t,si} dx + \sum \int_{0.115}^{0.13} \bar{q}_{t,si} dx}{\sum \int_{0.1}^{0.115} \bar{q}_{t,si} dx} \quad (12)$$

where $\bar{q}_{t,si}$ are the transversal heat fluxes at the stack surfaces. At $\Gamma_2 = 2.2$, η is estimated to be 5.45%.

Figure 16 further displays the dependence of η on Γ . It is found that η increases with increasing Γ , and there is no obvious bifurcation. In the figure, η is small which means only a small portion of heat is converted into acoustic power in the stack region. It should be noted that η is low in this study partly because the TAE is not loaded: the acoustic power generated in the stack is only used to overcome the thermal and viscous losses. η is often expected to be higher if an acoustic load such as a transducer is coupled with the TAE.

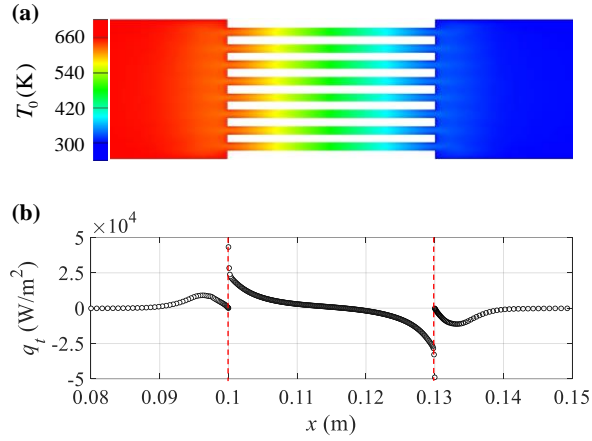


Figure 15. (a) Contour of time-averaged mean temperature of the fluid and (b) time-averaged surface heat flux distribution around the stack region at $\Gamma_2 = 2.2$.

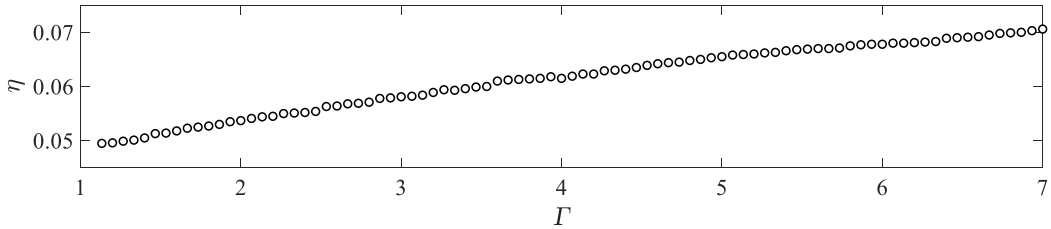


Figure 16. Dependence of thermal-to-acoustic efficiency η of the stack on Γ .

4. Parametric studies

Parametric studies to investigate the effect of the gap between stack plates and stack position on mode transition are described in this section. In the parametric studies, d_s (while maintaining $d_s = t_s$) or L_H

(while maintaining $L_H + L_R = 0.47$ m) is the varying parameter while the other geometrical parameters in Table 1 are fixed. In addition, Γ is kept constant at $\Gamma_4 = 3.6$.

4.1 Effect of gap between stack plates

Figure 17 displays p_{\max} for the steady-state response and the corresponding spectral map when d_S is chosen to be 0.87, 0.952, 1.053, 1.176, 1.333, 1.538 and 1.818 mm, with the number of gas channels being 11, 10, 9, 8, 7, 6 and 5, respectively. Three different regions are identified: in region G-I, second-mode limit-cycle oscillations dominate; in region G-II, quasiperiodicity takes place; in region G-III, first-mode limit-cycle oscillations dominate. In standing-wave TAEs, r_h / δ_k has an optimal value around 1.5 [51] to achieve maximum $\Delta \bar{I}$, with $r_h = d_S / 2$ being the hydraulic radius and $\delta_k = (2\kappa / \rho_0 c_p \omega)^{0.5}$ being the thermal penetration depth. Thus, a smaller value of d_S requires a higher ω to achieve an optimal r_h / δ_k . It is also interesting to find that p_{\max} for the second mode (region G-I) is smaller than that for the first mode (region G-III). A possible reason for this is that the viscous and thermal losses within the boundary layers increase with ω . The increase of viscous and thermal losses limits the growth of p_A during nonlinear saturation. In region G-II, the superposition of the first two modes leads to a sudden increase of p_{\max} . When $d_S = 1.176$ mm, p_{\max} is higher due to a relatively higher proportion of first-mode component compared to that when $d_S = 1.053$ mm.

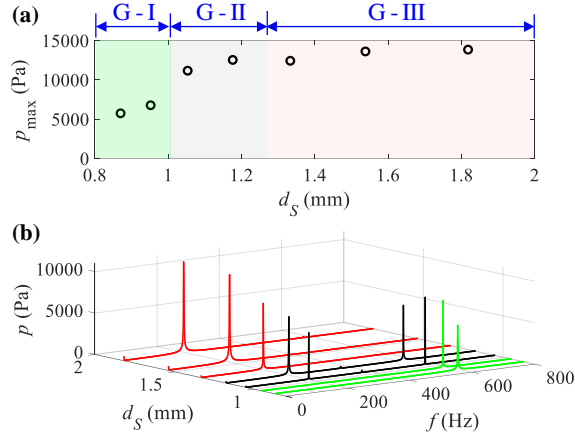


Figure 17. Effect of the gap d_S on the steady-state response. (a) Bifurcation diagram. The division of region G-I, G-II and G-III has a coarse resolution due to limited cases simulated. (b) Spectral map.

4.2 Effect of stack position

Figure 18 displays p_{\max} for the steady-state response and the corresponding spectral map when L_H is chosen to be 0.05, 0.1, 0.15, 0.2, 0.25, 0.3, 0.35 and 0.4 m. Three different regions are identified: second-mode limit cycle, quasiperiodic oscillations and first-mode limit cycle exist in regions P-I, P-II and P-III, respectively. In standing-wave TAEs, apart from r_h / δ_k , $\Delta \bar{I}$ is also affected by the amplitude of p and u . Thereby, to achieve maximum $\Delta \bar{I}$, the stack should be placed between the pressure and velocity antinodes. Referring to Figure 1(c), when $L_H = 0.05$ m, the stack is located near the pressure

antinode of the first mode, but between the pressure and velocity antinodes of the second mode. Thus, the second mode is more prone to instability. Another interesting finding is that p_{\max} decreases gradually as L_H increases in region P-III. Two reasons may account for this behaviour. On the one hand, the stack is moving towards the pressure node, leading to smaller $\Delta \bar{I}$. On the other hand, since the viscous boundary layer $\delta_v = (2\mu / \rho_0 \omega)^{0.5}$ is thicker in the hot buffer with a surface temperature T_h , the increase in L_H will cause larger viscous losses that significantly reduce p_{\max} .

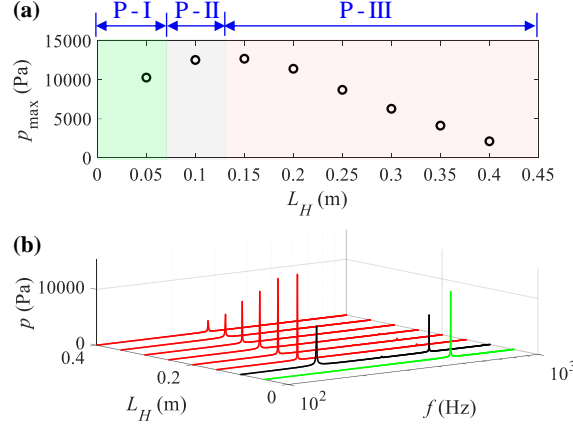


Figure 18. Effect of stack position on steady-state responses. (a) Bifurcation diagram. The division of region P-I, P-II and P-III has a coarse resolution due to limited cases simulated. (b) Spectral map.

5. Conclusions

This article numerically investigated the mode transition in a standing-wave thermoacoustic engine (TAE). Computational fluid dynamics (CFD) simulations were conducted to reproduce the mode transition phenomenon that has been observed in previous experimental studies, but not interpreted in theoretical or numerical ways. This research not only sheds light on the underlying mechanism of mode transition in standing-wave TAEs but also provides useful guidelines for controlling the dynamics of thermoacoustic oscillations. The key findings from this study are concluded as follows.

- (1) With the increase of temperature ratio Γ , a series of bifurcations in the nature of steady-state dynamics were observed, through which the TAE exhibited first-mode periodic oscillations, quasiperiodic oscillations and second-mode periodic oscillations. The wavelet transforms, bifurcation diagrams and spectral maps are useful tools to identify different dynamic regions and describe the mode transition process.
- (2) Dynamic mode decomposition (DMD) of the acoustic pressure in the initial decay or build-up demonstrates the onset of the first and/or second modes as Γ increases. The oscillation frequencies ω_R and growth/attenuation rates ω_I were obtained from both CFD simulations and linear theory, and good agreement was achieved between them. During saturation, nonlinear mode competition could result in the death of one acoustic mode caused by the other, even though it was initiated at

the beginning of the simulation. At steady state, periodic oscillations exhibit a closed loop in the phase space whilst quasiperiodic oscillations generate a torus. The time-averaged acoustic energy density \bar{w} and acoustic intensity generation $\Delta \bar{I}$ versus Γ agree with the pressure maxima p_{\max} versus Γ except at the 2nd and 3rd bifurcation points due to the incoherence of acoustic waves at incommensurate frequencies.

- (3) Parametric studies on the effect of the gap between stack plates and stack position indicate that at a large Γ , the TAE will exhibit second-mode oscillations when the gap is small or when the stack is close to the closed end. This is due to the fact that $I = pu$ (non-zero within the boundary layers) is affected by both r_h / δ_k and $|p_1||u_1|$. r_h / δ_k is close to the optimal value at small gaps and the second mode; $|p_1||u_1|$ for the second mode is large when the stack is placed between the pressure and velocity antinodes near the closed end.
- (4) The mode transition could be potentially utilized to achieve a better matching between the TAE and external loads. For example, for linear alternators which normally resonate at low frequencies, the TAE should be working at the fundamental mode. For piezoelectric transducers that normally have high resonant frequencies, the second mode should be encouraged. Hence, we can control the oscillation frequency of the TAE to be in resonance with the external loads to achieve higher electric power outputs.

The CFD methodology in this research proves effective in simulating the mode transition in standing-wave TAEs. Future work may involve the application of this numerical approach to simulate the mode transition/competition in more efficient travelling-wave thermoacoustic devices.

Acknowledgements

High-performance computing (HPC) provided by New Zealand eScience Infrastructure (NeSI) is acknowledged. The authors are grateful for the financial support from China Scholarship Council (no. 201608630046) and the Universitas 21 Doctoral Student Mobility Scholarship from the University of Auckland.

Conflict of interest

There is no conflict of interest declared by the authors.

Appendix A. Two-port reduced-order network model

Swift [1] linearized the nonlinear governing equations in fluidic mechanics by assuming that every oscillating variable can be expressed as $\Phi(x,t) = \Phi_0 + \Re [\Phi_1(x)e^{j\omega t}]$, where subscripts 0 and 1 represent the mean and first-order fluctuation (in complex notation) components. $\Re[\]$ signifies the real part of a complex quantity and $e^{j\omega t}$ denotes harmonic time dependence. The momentum and continuity equations in the linearized form are

$$\frac{dp_1}{dx} = -\frac{j\omega\rho_0}{A(1-f_v)}U_1 = -(j\omega l + r_v)U_1 \quad (\text{A1})$$

$$\frac{dU_1}{dx} = -(1+(\gamma-1)f_k)\frac{j\omega A}{\gamma p_0}p_1 + \frac{f_k-f_v}{(1-\sigma)(1-f_v)}\frac{1}{T_0}\frac{dT_0}{dx}U_1 = -\left(j\omega c + \frac{1}{r_k}\right)p_1 + gU_1 \quad (\text{A2})$$

where U is the volume velocity and γ is the specific heat ratio. f_v and f_k are thermo-viscous functions accounting for the viscous and thermal-relaxation effects within the boundary layers [52], while

$$c = \frac{A}{\gamma p_0}(1+(\gamma-1)\Re[f_k]), \quad l = \frac{\rho_0}{A}\frac{1-\Re[f_v]}{|1-f_v|^2} \quad (\text{A3})$$

represent the acoustic compliance and inertance per unit length, respectively. Furthermore,

$$\frac{1}{r_k} = \frac{\gamma-1}{\gamma}\frac{\omega A \Im[-f_k]}{p_0}, \quad g = \frac{f_k-f_v}{(1-f_v)(1-\sigma)}\frac{1}{T_0}\frac{dT_0}{dx}, \quad r_v = \frac{\omega\rho_0}{A}\frac{\Im[-f_v]}{|1-f_v|^2} \quad (\text{A4})$$

represent the thermal-relaxation resistance per unit length, complex gain/attenuation constant due to a non-zero temperature gradient and viscous resistance per unit length, respectively. $\Im[\cdot]$ signifies the imaginary part of a complex quantity.

Lump the oscillatory fluid inside the TAE into a large number of small elements of length Δx . Each element can be represented by an equivalent circuit as shown in Figure A1. Then, the acoustic pressure and volume velocity at the ends of each element can be related by a transfer matrix \mathbf{T}_1 , so that

$$\begin{bmatrix} p(i+1) \\ U_1(i+1) \end{bmatrix} = \mathbf{T}_1 \begin{bmatrix} p_1(i) \\ U_1(i) \end{bmatrix} = \begin{bmatrix} 1 & -j\omega l(i)\Delta x - r_v(i)\Delta x \\ -j\omega c(i)\Delta x - \frac{1}{r_k(i)}\Delta x & g(i)\Delta x + 1 \end{bmatrix} \begin{bmatrix} p_1(i) \\ U_1(i) \end{bmatrix} \quad (\text{A5})$$

By assuming continuity of at the interfaces between two adjacent elements, the acoustic pressure and volume velocity at the ends of the TAE can be related by a total transfer matrix $\mathbf{T}_T = \mathbf{T}_R \mathbf{T}_S \mathbf{T}_H$, where \mathbf{T}_H , \mathbf{T}_S and \mathbf{T}_R are the products of the transfer matrices of all the lumped elements in the hot buffer, stack and resonator respectively. Hence,

$$\begin{bmatrix} p_1(L) \\ U_1(L) \end{bmatrix} = \mathbf{T}_T \begin{bmatrix} p_1(0) \\ U_1(0) \end{bmatrix} \quad (\text{A6})$$

Define $Z(0) = p_1(0) / U_1(0)$ and $Z(L) = p_1(L) / U_1(L)$. Equation (A6) can be rewritten as

$$Z(L) = \frac{-T_{r11}Z(0) + T_{r12}}{-T_{r21}Z(0) + T_{r22}} \quad (\text{A7})$$

where T_{T11} , T_{T12} , T_{T21} and T_{T22} are the four elements of matrix \mathbf{T}_T . Since $U_1(0) = p_1(L) = 0$ in the CFD simulations, the characteristic equation (A7) reduces to

$$T_{T11} = 0 \quad (\text{A8})$$

Solving Equation (A8) yields the eigenvalue (complex frequency $\omega = \omega_R + j\omega_I$) at any specified L .

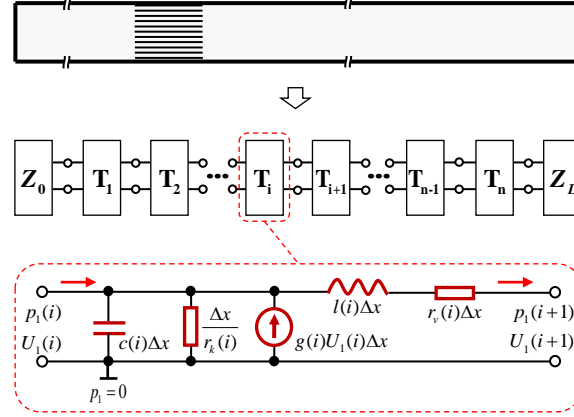


Figure A1. Two-port reduced-order network model of the TAE.

References

- [1] G.W. Swift, *Thermoacoustics: A unifying perspective for some engines and refrigerators*, Springer, 2017.
- [2] T. Jin, J. Huang, Y. Feng, R. Yang, K. Tang, R. Radebaugh, Thermoacoustic prime movers and refrigerators: Thermally powered engines without moving components, *Energy*, 93 (2015) 828-853.
- [3] M.A. Timmer, K. de Blok, T.H. van der Meer, Review on the conversion of thermoacoustic power into electricity, *The Journal of the Acoustical Society of America*, 143 (2018) 841-857.
- [4] L. Tartibu, Developing more efficient travelling-wave thermo-acoustic refrigerators: A review, *Sustainable Energy Technologies and Assessments*, 31 (2019) 102-114.
- [5] J. Xu, J. Hu, E. Luo, L. Zhang, W. Dai, A cascade-looped thermoacoustic driven cryocooler with different-diameter resonance tubes. Part I: Theoretical analysis of thermodynamic performance and characteristics, *Energy*, 181 (2019) 943-953.
- [6] J. Xu, J. Hu, Y. Sun, H. Wang, Z. Wu, J. Hu, S. Hochgreb, E. Luo, A cascade-looped thermoacoustic driven cryocooler with different-diameter resonance tubes. Part II: Experimental study and comparison, *Energy*, 207 (2020) 118232.
- [7] J. Xu, E. Luo, S. Hochgreb, Study on a heat-driven thermoacoustic refrigerator for low-grade heat recovery, *Applied Energy*, 271 (2020) 115167.
- [8] C.J. Lawn, G. Penelet, Common features in the thermoacoustics of flames and engines, *International Journal of Spray and Combustion Dynamics*, (2017) 1756827717743911.
- [9] H. Hao, C. Scalo, F. Semperlotti, Traveling and standing thermoacoustic waves in solid media, *Journal of Sound and Vibration*, 449 (2019) 30-42.
- [10] H. Hao, C. Scalo, F. Semperlotti, Axial-mode solid-state thermoacoustic instability: An analytical parametric study, *Journal of Sound and Vibration*, 470 (2020) 115159.
- [11] G.W. Swift, Thermoacoustic engines, *The Journal of the Acoustical Society of America*, 84 (1988) 1145-1180.

- [12] A. Piccolo, Numerical study of entropy generation within thermoacoustic heat exchangers with plane fins, *Entropy*, 17 (2015) 8228-8239.
- [13] F. Auriemma, E.D. Giulio, M. Napolitano, R. Dragonetti, Porous Cores in Small Thermoacoustic Devices for Building Applications, *Energies*, 13 (2020) 2941.
- [14] P.H. Ceperley, A pistonless Stirling engine—The traveling wave heat engine, *The Journal of the Acoustical Society of America*, 66 (1979) 1508-1513.
- [15] K. Wang, S. Dubey, F.H. Choo, F. Duan, Thermoacoustic Stirling power generation from LNG cold energy and low-temperature waste heat, *Energy*, 127 (2017) 280-290.
- [16] T. Biwa, D. Hasegawa, T. Yazaki, Low temperature differential thermoacoustic Stirling engine, *Applied physics letters*, 97 (2010) 034102.
- [17] Z. Yu, A.J. Jaworski, S. Backhaus, Travelling-wave thermoacoustic electricity generator using an ultra-compliant alternator for utilization of low-grade thermal energy, *Applied Energy*, 99 (2012) 135-145.
- [18] J. Tan, J. Luo, Y. Wang, J. Wei, T. Jin, Performance of an air - cooled looped thermoacoustic engine capable of recovering low - grade thermal energy, *International Journal of Energy Research*, (2020).
- [19] R. Yang, Y. Wang, Y. Feng, T. Jin, K. Tang, Performance of a looped thermoacoustic engine with multiple loads capable of utilizing heat source below 200° C, *Applied Thermal Engineering*, 148 (2019) 516-523.
- [20] R. Yang, Y. Wang, J. Luo, J. Tan, T. Jin, Performance comparison of looped thermoacoustic electric generators with various thermoacoustic stages, *International Journal of Energy Research*, (2019).
- [21] Z. Yu, Q. Li, X. Chen, F. Guo, X. Xie, J. Wu, Investigation on the oscillation modes in a thermoacoustic Stirling prime mover: mode stability and mode transition, *Cryogenics*, 43 (2003) 687-691.
- [22] T. Yazaki, S. Takashima, F. Mizutani, Complex quasiperiodic and chaotic states observed in thermally induced oscillations of gas columns, *Physical review letters*, 58 (1987) 1108.
- [23] T. Yazaki, Experimental observation of thermoacoustic turbulence and universal properties at the quasiperiodic transition to chaos, *Physical Review E*, 48 (1993) 1806.
- [24] A.A. Atchley, F.m. Kuo, Stability curves for a thermoacoustic prime mover, *The Journal of the Acoustical Society of America*, 95 (1994) 1401-1404.
- [25] V.R. Unni, Y.M. Prasaad, N. Ravi, S.M. Iqbal, B. Pesala, R. Sujith, Experimental investigation of bifurcations in a thermoacoustic engine, *International Journal of Spray and Combustion Dynamics*, 7 (2015) 113-129.
- [26] T. Biwa, Y. Ueda, T. Yazaki, U. Mizutani, Thermodynamical mode selection rule observed in thermoacoustic oscillations, *EPL (Europhysics Letters)*, 60 (2002) 363.
- [27] G. Chen, L. Tang, Z. Yu, Underlying physics of limit-cycle, beating and quasi-periodic oscillations in thermoacoustic devices, *Journal of Physics D: Applied Physics*, 53 (2020) 215502.
- [28] G. Chen, L. Tang, Z. Yang, K. Tao, Z. Yu, An electret - based thermoacoustic - electrostatic power generator, *International Journal of Energy Research*, 44 (2020) 2298-2305.
- [29] J. Tan, J. Luo, J. Wei, T. Jin, Numerical and experimental study of a two-phase thermofluidic oscillator with regenerator achieving low temperature-differential oscillation, *Applied Thermal Engineering*, (2020) 115790.
- [30] Y. Ueda, C. Kato, Stability analysis of thermally induced spontaneous gas oscillations in straight and looped tubes, *The Journal of the Acoustical Society of America*, 124 (2008) 851-858.
- [31] C. Scalo, S.K. Lele, L. Hesselink, Linear and nonlinear modelling of a theoretical travelling-wave thermoacoustic heat engine, *Journal of Fluid Mechanics*, 766 (2015) 368-404.

- [32] A.I.A. El-Rahman, W.A. Abdelfattah, M.A. Fouad, A 3D investigation of thermoacoustic fields in a square stack, *International Journal of Heat and Mass Transfer*, 108 (2017) 292-300.
- [33] L. Liu, P. Yang, Y. Liu, Comprehensive performance improvement of standing wave thermoacoustic engine with converging stack: Thermodynamic analysis and optimization, *Applied Thermal Engineering*, 160 (2019) 114096.
- [34] A. Favre, *Equations des gaz turbulents compressibles*, J. de Mecanique, 4 (1965).
- [35] S.B. Pope, *Turbulent flows*, in, IOP Publishing, 2001.
- [36] B.E. Launder, D.B. Spalding, The numerical computation of turbulent flows, in: *Numerical prediction of flow, heat transfer, turbulence and combustion*, Elsevier, 1983, pp. 96-116.
- [37] G. Chen, G. Krishan, Y. Yang, L. Tang, B. Mace, Numerical investigation of synthetic jets driven by thermoacoustic standing waves, *International Journal of Heat and Mass Transfer*, 146 (2020) 118859.
- [38] G. Chen, L. Tang, B.R. Mace, Bistability and triggering in a thermoacoustic engine: A numerical study, *International Journal of Heat and Mass Transfer*, 157 (2020) 119951.
- [39] G. Yu, W. Dai, E. Luo, CFD simulation of a 300Hz thermoacoustic standing wave engine, *Cryogenics*, 50 (2010) 615-622.
- [40] W. Sutherland, LII. The viscosity of gases and molecular force, *The London, Edinburgh, and Dublin Philosophical Magazine and Journal of Science*, 36 (1893) 507-531.
- [41] D. Zhao, Y. Chew, Energy harvesting from a convection-driven Rijke-Zhao thermoacoustic engine, *Journal of Applied Physics*, 112 (2012) 114507.
- [42] G. Chen, Y. Wang, L. Tang, K. Wang, Z. Yu, Large eddy simulation of thermally induced oscillatory flow in a thermoacoustic engine, *Applied Energy*, 276 (2020) 115458.
- [43] A. Grossmann, R. Kronland-Martinet, J. Morlet, Reading and understanding continuous wavelet transforms, in: *Wavelets*, Springer, 1990, pp. 2-20.
- [44] M. Lakshmanan, S. Rajaseekar, *Nonlinear dynamics: integrability, chaos and patterns*, Springer Science & Business Media, 2012.
- [45] M. Guedra, G. Penelet, On the use of a complex frequency for the description of thermoacoustic engines, *Acta Acustica united with Acustica*, 98 (2012) 232-241.
- [46] G. Chen, L. Tang, B.R. Mace, Modelling and analysis of a thermoacoustic-piezoelectric energy harvester, *Applied Thermal Engineering*, 150 (2019) 532-544.
- [47] G. Chen, L. Tang, B.R. Mace, Theoretical and experimental investigation of the dynamic behaviour of a standing-wave thermoacoustic engine with various boundary conditions, *International Journal of Heat and Mass Transfer*, 123 (2018) 367-381.
- [48] H. Abarbanel, *Analysis of observed chaotic data*, Springer Science & Business Media, 2012.
- [49] Y. Sun, Z. Rao, D. Zhao, B. Wang, D. Sun, X. Sun, Characterizing nonlinear dynamic features of self-sustained thermoacoustic oscillations in a premixed swirling combustor, *Applied Energy*, 264 (2020) 114698.
- [50] S.H. Strogatz, *Nonlinear dynamics and chaos with student solutions manual: With applications to physics, biology, chemistry, and engineering*, CRC press, 2018.
- [51] Z. Yu, A. Jaworski, Optimization of thermoacoustic stacks for low onset temperature engines, *Proceedings of the Institution of Mechanical Engineers, Part A: Journal of Power and Energy*, 224 (2010) 329-337.
- [52] W.P. Arnott, H.E. Bass, R. Raspet, General formulation of thermoacoustics for stacks having arbitrarily shaped pore cross sections, *The Journal of the Acoustical Society of America*, 90 (1991) 3228-3237.